RSC Advances

PAPER

View Article Online
View Journal | View Issue

Cite this: *RSC Adv.*, 2021, **11**, 8993

Electrochemical investigation and amperometry determination iodate based on ionic liquid/polyoxotungstate/P-doped electrochemically reduced graphene oxide multi-component nanocomposite modified glassy carbon electrode†

Minoo Sharifi, Somayeh Dianat* and Amin Hosseinian

A novel modified glassy carbon electrode (GCE) was successfully fabricated with a tetra-component nanocomposite consisting of (1,1′-(1,4-butanediyl)dipyridinium) ionic liquid (bdpy), $SiW_{11}O_{39}Ni(H_2O)$ ($SiW_{11}Ni$) Keggin-type polyoxometalate (POM), and phosphorus-doped electrochemically reduced graphene oxide (P-ERGO) by electrodeposition technique. The (bdpy)$SiW_{11}Ni$/GO hybrid nanocomposite was synthesized by a one-pot hydrothermal method and characterized by UV-vis absorption, Fourier transform infrared (FT-IR) spectroscopy, X-ray diffraction (XRD) analysis, thermogravimetric-differential thermal analysis (TGA/DTA), and transmission electron microscopy (TEM). The morphology, electrochemical performance, and electrocatalysis activity of the nanocomposite modified glassy carbon electrode ((bdpy)$SiW_{11}Ni$/P-ERGO/GCE) were analyzed by field emission scanning electron microscopy (FE-SEM) coupled with energy-dispersive X-ray spectroscopy (EDS), cyclic voltammetry (CV), square wave voltammetry (SWV), and amperometry, respectively. Under the optimum experimental conditions, the as-prepared sensor showed high sensitivity of 28.1 μA mM^{-1} and good selectivity for iodate (IO_3^-) reduction, enabling the detection of IO_3^- within a linear range of 10–1600 μmol L^{-1} (R^2 = 0.9999) with a limit of detection (LOD) of 0.47 nmol L^{-1} (S/N = 3). The proposed electrochemical sensor exhibited good reproducibility, and repeatability, high stability, and excellent anti-interference ability, as well as analytical performance in mineral water, tap water, and commercial edible iodized salt which might provide a capable platform for the determination of IO_3^-.

Received 31st January 2021
Accepted 22nd February 2021

DOI: 10.1039/d1ra00845e

rsc.li/rsc-advances

1. Introduction

Polyoxometalates (POMs) are a family of anionic nanoclusters consisting of early transition metals and oxygen atoms to form a closed 3-dimensional framework.[1,2] POMs, especially Keggin-type POMs, have different applications in the fields of catalysis,[3–6] medicine,[7–9] and molecular materials[10,11] due to their excellent redox character, unique molecular structure, electronic versatility, and easy preparation. One of the attractive properties of POMs is that the anionic cluster can undergo a fast, stepwise, reversible, and multi-electron transfer reaction while keeping the structural integrity.[2,12–14] The multiple redox properties make them attractive candidates in surface modification, electroanalysis, and electrocatalysis.[2,13–15]

Different methods have been developed to achieve chemically modified electrodes (CMEs) with POMs such as electrodeposition at a very negative potential,[16,17] adsorption,[18] entrapment into conducting,[19,20] or non-conducting polymers matrixes,[21,22] layer-by-layer self-assembly,[23,24] Langmuir–Blodgett (LB) technique,[25,26] preparation of self-assembled monolayer and multilayer thin-films,[27] and bulk modification of carbon composites and carbon paste matrices.[28] However, the electrocatalytic activity of POMs-modified electrodes is limited due to their low stability in aqueous solutions[15,27,29] and low specific surface area.[30]

To achieve the enhanced stability of POMs, many studies have been focused on the design and construction of modifying and assemble POMs with suitable organic matrices, which is one of the most exciting fields in the materials chemistry.[27,31–33] Recently, ionic liquids (ILs) have concerned more attention,[34–36] due to owning highlight properties such as good aqueous solubility, high electrical conductivity, non-volatility, non-flammability, low toxicity, high thermal and electrochemical stabilities, and large electrochemical potential window.[37]

Furthermore, immobilization or dispersion of POMs on different supporting carbon materials has attracted significant attention due to their small background currents, wide

Department of Chemistry, Faculty of Sciences, University of Hormozgan, Bandar Abbas 79161-93145, Iran. E-mail: s.dianat@hormozgan.ac.ir; Tel: +98 76 33670121

† Electronic supplementary information (ESI) available. See DOI: 10.1039/d1ra00845e

potential windows, low-cost, excellent chemical stability, and a strong affinity for POMs.[38–43]

Graphene was discovered in 2004 as a new carbon nanostructure by Novoselov and Geim.[44] Graphene is a two-dimensional (2D) crystal composed of a monolayer of sp^2 hybridized carbon atoms arranged in a hexagonal packing structure.[45] Graphene is the thinnest and strongest material known to exist in the world.[46] Graphene has been widely studied in the nanotechnology and nanoscience applications due to exclusive properties such as good chemical stability, great specific surface area (SSA, about 2600 $m^2\ g^{-1}$), high electron mobility, and good thermal conductivity.[13] Graphene is a proper candidate for a POM support material to solve both high solubility and low surface area of POMs.[47] Moreover, the interesting properties of POMs, particularly as catalysis,[48,49] electrocatalysis,[50,51] and capacitance[52,53] can be improved by the large SSA and good conductivity of graphene. So far, many studies have been reported on POM/graphene nanocomposites, in which graphene oxide (GO) is applied as support and POMs are immobilized onto the reduced GO (RGO) through various reduction methods such as UV-photoreduction,[54–57] and chemical reduction with the help of hazardous substances (*e.g.*, hydrazine).[58] However, these methods generally obtained powder POM/RGO nanocomposites that need to be deposited on the electrode surface using the drop-casting technique. This preparation method has intrinsic limitations such as low stability and lack of control of the film thickness.[59,60] The self-assembly technique is the best method for the construction of the stable and uniform modified surfaces. In some research, POM/RGO nanocomposite is prepared through the layer-by-layer electrostatic assembly of POM/GO followed by the UV-photoreduction step.[24,61] Lately, the electrochemical reduction of GO to RGO has attracted great attention due to its green and simple preparation method.[59,60,62,63] Chen *et al.* deposited RGO on the surface of a glassy carbon electrode (GCE) by cyclic voltammetric (CV) reduction of a GO colloidal solution, which presented the high-resolution ability to the catechol and hydroquinone isomers.[60] Weihua Guo *et al.* reported the preparation and electrocatalytic activity of Keggin-type heteropolymolybdate $H_4SiMo_{12}O_{40}$ and chitosan-electrochemically RGO multilayer composite films on indium tin oxide electrode (ITO) for determination of $S_2O_8^{2-}$ with excellent sensitivity and a low detection limit.[59] Mai *et al.* reported the preparation of RGO/copper composite from a surfactant-free colloidal solution comprised of $[Cu^{II}EDTA]^{2-}$ complexes and GO sheets by electrochemical reduction.[62] Recently, many studies have confirmed that doping of heteroatoms can well modify the electronic structure and enhance the electrochemical properties of RGO. For instance, boron, nitrogen, phosphorus, and sulfur atoms doped into graphene can improve the electrical conductivity and electrocatalytic activity of RGO, which can be applied as high-performance supercapacitor electrode,[64,65] lithium-ion batteries,[66–69] fuel cells,[70,71] and dye-sensitized solar cells.[72] Although the electrochemical reduction method has many advantages in preparing of the P-doped graphene monolayer film modified electrode, few studies have been reported concerning the modified electrode with POM/P-ERGO and its derivatives prepared by this method. Using the electrochemical reduction method for the fabrication of the POM/P-ERGO modified electrode still has challenges.

In this study, a new organic–inorganic nanocomposite (1,1′-(1,4-butanediyl)dipyridinium)$_3$ $[SiW_{11}O_{39}Ni(H_2O)]$/GO has been processed on GCE through electrochemical reduction method ((bdpy)SiW_{11}Ni/P-ERGO/GCE). For this purpose, (bdpy)SiW_{11}Ni/GO nanohybrid compound was deposited on a GCE by one-step drop-casting, followed by the electrochemical reduction of GO through chronoamperometry at a constant potential of −1.5 V (*vs.* Ag/AgCl), for 60 s, in a phosphoric acid solution (0.1 mol L^{-1}) containing bdpy (1.0 mmol L^{-1}). (bdpy)SiW_{11}Ni can interact with P-ERGO *via* $P^{\delta+}$ and π-electrons of bdpy without affecting the electronic structure of POM. Consequently, the presence of bdpy provides an additional advantage for increasing the loading of POM and improving the stability of nanocomposite film due to the strong electrostatic attraction between $[SiW_{11}Ni]^{6-}$ and positively charged bdpy. Then, electrochemical and electrocatalytic behaviors, selectivity, repeatability, reproducibility of the proposed sensor for iodate (IO_3^-) determination, and also the recovery in the mineral water, tap water, and a commercial edible iodized salt were investigated.

2. Experiment

2.1. Materials and reagents

The $K_6[SiW_{11}O_{39}Ni(H_2O)]\cdot nH_2O$ ($SiW_{11}Ni$) was synthesized according to the previous literature.[73] Tungstosilicic acid hydrate ($H_4SiW_{12}O_{40}\cdot nH_2O$, HSiW), potassium acetate (CH_3COOK), nickel(II) nitrate hexahydrate ($Ni(NO_3)_2\cdot 6H_2O$), 1,1′-(1,4-butanediyl)dipyridinium dibromide (bdpy) ionic liquid, glacial acetic acid (CH_3COOH), phosphoric acid (H_3PO_4), sulfuric acid (H_2SO_4), graphite powder (<20 μm), ethanol (C_2H_5OH), methanol (CH_3OH), hydrogen peroxide (H_2O_2), potassium permanganate ($KMnO_4$), potassium hexacyanoferrate(III) ($K_3[Fe(CN)_6]$), and potassium iodate (KIO_3) with analytical grade were commercially purchased from Sigma or Merck companies. All solutions were prepared with deionized water (18 MΩ cm (25 °C), Milli Q, Millipore Inc.).

2.2. Apparatus

Attenuated total reflectance-Fourier transform infrared (ATR-FTIR) spectra were acquired on a Spectrum Two spectrometer-PerkinElmer in the 2400–400 cm^{-1} wavenumber range. UV-vis absorption spectra of the $SiW_{11}Ni$, bdpy and (bdpy)SiW_{11}Ni were recorded using a Unico SQ-4802 double beam UV-vis spectrophotometer in a 1 cm matched quartz cell. The crystalline structures of the $SiW_{11}Ni$, bdpy, (bdpy)SiW_{11}Ni, GO, and (bdpy)SiW_{11}Ni/GO were investigated by an X-ray diffraction technique (XRD, Panalytical X'pert PRO, The Netherlands) using Cu Kα radiation. The thermal features of bdpy, $SiW_{11}Ni$, and (bdpy)SiW_{11}Ni/GO were evaluated using thermogravimetric/differential thermal analysis (TGA/DTA, Rheometric Scientific STA 1500) under air flow in the temperature range of 25–800 °C at a heating rate of 10 °C min^{-1}. Transmission electron microscope (TEM, EM10C-100 kV series,

Zeiss Co., Germany) was used to study and compare the morphology of the (bdpy)$SiW_{11}Ni$/GO with GO. The morphology and elemental analysis of the bare GCE and (bdpy)$SiW_{11}Ni$/P-RGO/GCE were analyzed by field emission scanning electron microscopy (FE-SEM, SIGMA VP, Zeiss Co., Germany), coupled with energy-dispersive X-ray spectrometry (EDS) and EDS-mapping.

2.3. Electrochemical measurements

The electrochemical measurements were carried out using an Autolab potentiostat (P/GSTAT 302N, Metrohm Autolab Eco-Chemie Utrecht, The Netherlands) equipped with GPES, version 4.9. A conventional three-electrode system was employed containing bare or modified GCE (GR-2S/N, Iran, Tehran, diameter 2 mm), an Ag/AgCl (3 mol L^{-1} KCl) electrode (Metrohm, Switzerland), and a platinum rod (IV-EL/EB-2200, Ivium, Eindhoven, The Netherlands) as working, reference and counter electrodes, respectively. Prior to the electrochemical experiments, high-purity argon gas (99.999%) was purged into the electrolytic cell solutions for 10 minute and covered by the Ar-atmosphere during the experiments. All experiments were done at ambient temperature.

2.4. Preparation of $(bdpy)_3[SiW_{11}O_{39}Ni(H_2O)]\cdot nH_2O$ ((bdpy)$SiW_{11}Ni$)

First, a solution of 14.0 g of HSiW (4.72 mmol) in 50 mL distilled water at 95 °C was prepared. Then, a hot solution of 1.1 g $Ni(NO_3)_2\cdot 6H_2O$ (6.05 mmol) in 10 mL distilled water was added drop by drop, followed by a solution of 15.0 g CH_3COOK in 15 mL hot distilled water (pH regulated to 7 with acetic acid). The stirred solution was kept at 95 °C for one minute and was quickly filtered. Then, the filtrate was cooled to 50 °C, and an equal volume of methanol was added. In continuous, solid bdpy ionic liquid was gradually added into the solution until no more precipitate formed. Finally, the light green powders of (bdpy)$SiW_{11}Ni$ were filtered, well washed with ethanol and diethyl ether, and dried at room temperature (yield ~ 85%).

2.5. Preparation of (bdpy)$SiW_{11}Ni$/GO

GO was obtained from graphite powder using modified Hummer's method.[74] A suspension of 30 mg GO in 10 mL of distilled water was prepared, followed by sonication (30 min) to form a uniform suspension. Then 1.5 g of (bdpy)$SiW_{11}Ni$ (0.34 mmol) was added. After sonication (20 min), the mixture was poured into a 100 mL Teflon-lined stainless-steel autoclave. The autoclave was transferred to an oven at 180 °C for 24 h. The obtained black precipitation ((bdpy)$SiW_{11}Ni$/GO) was washed with distilled water and dried at 60 °C for 12 h in a vacuum oven.

2.6. Fabrication of (bdpy)$SiW_{11}Ni$/P-ERGO/GCE

Before the electrode modification, the bare GCE was cleaned by polishing with 0.30 μm, 0.10 μm, and 0.05 μm α-Al_2O_3 slurries to elimination the adsorbed impurities. The polished electrode was sonicated in deionized water, ethanol, and deionized water bath, respectively, each for 5 minute. Then the GCE was treated with 0.5 mol L^{-1} H_2SO_4 solution by repeated cycling in the potential range from −1.0 to 1.0 V (*vs.* Ag/AgCl) until a stable CV was obtained, followed by the rinsing with deionized water and natural drying at room temperature. Next, 10 mg of as-prepared (bdpy)$SiW_{11}Ni$/GO nanocomposite was dispersed in 5 mL of ethanol and sonicated for 30 minutes to get a homogenously dispersed solution. 5 μL of the (bdpy)$SiW_{11}Co$/GO suspension was drop-casted on the cleaned bare GCE, and the solvent was removed under room temperature and washed with deionized water. Then, electrochemical reduction of GO to RGO was performed in 0.1 mol L^{-1} H_3PO_4 containing various concentrations of bdpy (0.5, 1.0, 5.0, and 10.0 mmol L^{-1}) using chronoamperometry in the potential of −1.5 V at different times (30, 60, 90, and 120 s). A better analytical signal obtained in the presence of 1.0 mmol L^{-1} bdpy and at time 60 s. Hence,

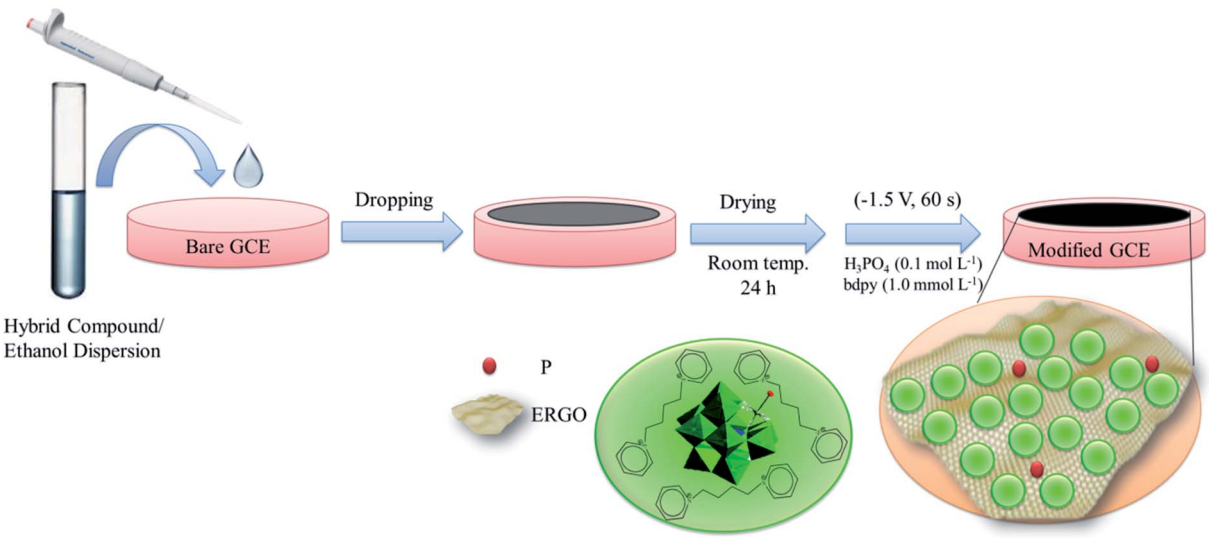

Scheme 1 Schematic diagram of stepwise electrode modification processes.

1.0 mmol L^{-1} bdpy and time 60 s were used as optimum factors in the fabrication of the modified working electrode in all studies. For comparison, $SiW_{11}Ni$/GCE, bdpy/GCE, (bdpy)$SiW_{11}Ni$/GCE, and P-ERGO/GCE were prepared by the same method. The schematic illustration of the preparation procedure of the as-prepared modified electrode is shown in Scheme 1.

2.7. Electrochemical procedure

The electrochemical measurements were carried out in a 90 mL electrochemical cell, containing 5 mL of $HClO_4$ (0.1 mol L^{-1}, pH 1.5) solution and various concentrations of IO_3^-. All the solutions within the cell were purged with high-pure argon for 10 minute before to the electrochemical analysis. The CV, square wave voltammetry (SWV), and amperometry techniques were used for the investigation of electrochemical behavior and electrocatalytic activity of the modified electrode in IO_3^- determination.

3. Results and discussion

3.1. Characterization

The carbon, nitrogen, silicon, tungsten, and nickel content of (bdpy)$SiW_{11}Ni$ were analyzed by elemental analysis. Calculated values [%]: C: 13.96; N: 2.32; Si: 0.78; W: 56.02; Ni: 1.63. Experimental values [%]: C: 13.75; N: 2.38; Si: 0.72; W: 52.71; Ni: 1.67. The obtained results approve that experimental values agree with the theoretical values calculated based on formula $(bdpy)_3SiW_{11}Ni$. Moreover, the molar ratios of Si : W : Ni = 1 : 11.2 : 1.1 prove that the Keggin structure of $SiW_{11}Ni$ has been retained throughout the functionalization with bdpy.

XRD analysis is done for the crystalline structure investigation of the (bdpy)$SiW_{11}Ni$/GO. The XRD patterns of $SiW_{11}Ni$, (bdpy)$SiW_{11}Ni$, bdpy, GO, and (bdpy)$SiW_{11}Ni$/GO are presented in Fig. 1. As displayed in Fig. 1b, (bdpy)$SiW_{11}Ni$ shows (001), and (002) diffraction peaks, which are located at 8.3°, and 16.5°, respectively of the $SiW_{11}Ni$ (Fig. 1a). Other obvious characteristic peaks, at 15.4°, and 20.2° can be credited to the bdpy ionic liquid (Fig. 1c). Fig. 1d is the XRD pattern of GO. Two relatively broad peaks are observed at 9.1° and 26.4°, which correspond to (001) and (002) reflections of GO and graphite existent in the structure of GO, respectively.[75,76] In Fig. 1e, the characteristic XRD peaks of (bdpy)$SiW_{11}Ni$/GO appeared at nearly similar locations without a significant shift in its peaks position compared to those of $SiW_{11}Ni$. Additionally, the characteristic peaks at 26.4° (002), confirmed that (bdpy)$SiW_{11}Ni$ was immobilized on the GO surface. However, the peak (001) was not observed due to the overlap with the peak of $SiW_{11}Ni$, which has a higher crystallinity.

The TGA/DTA diagrams for bdpy, $SiW_{11}Ni$, and (bdpy)$SiW_{11}Ni$/GO hybrid composite under the air atmosphere are shown in Fig. 2.

As shown in Fig. 2A, bdpy shows a significant weight loss of about 61.3% at the temperature range of 250–320 °C (3rd peak of the DTA curve) that can be credited to the decomposition of pyridine rings.

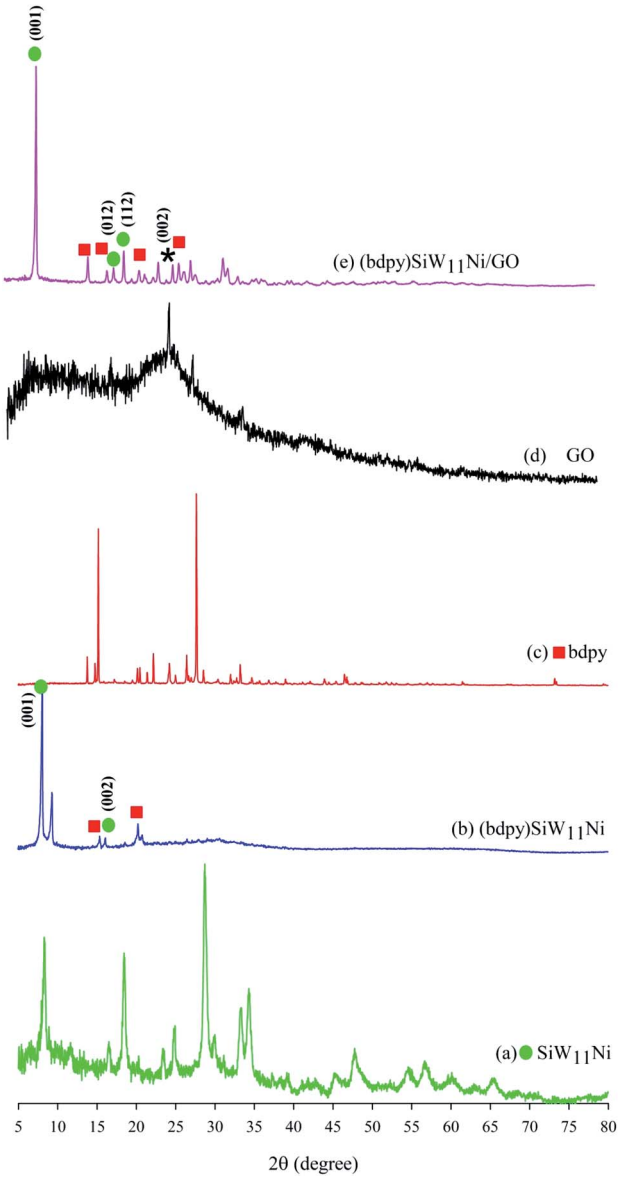

Fig. 1 XRD patterns of (a) $SiW_{11}Ni$, (b) (bdpy)$SiW_{11}Ni$, (c) bdpy, (d) GO, and (e) (bdpy)$SiW_{11}Ni$/GO.

The thermal analysis of $SiW_{11}Ni$ shows a slight weight loss (about 3.4%) at temperatures below 150 °C (1st peak of DTA), which may be related to eliminating adsorbed water molecules into $SiW_{11}Ni$ crystal lattice. A weight loss (about 13.2%) is observed in 150 to 384 °C temperature range during two steps (2nd and 3rd peak of DTA), which can be attributed to the removal water of crystallization from the crystal lattice of $SiW_{11}Ni$. Above 400 °C, no significant change in mass is observed, indicating its high thermal stability up to 800 °C (Fig. 2B).

As shown in Fig. 2C, the thermal stability of the (bdpy)$SiW_{11}Ni$/GO is entirely more than the parent bdpy but is slightly less than the original $SiW_{11}Ni$. Below 250 °C, no major change in weight loss was observed which confirms that the amount of water in the hybrid material was reduced but not eliminated. A

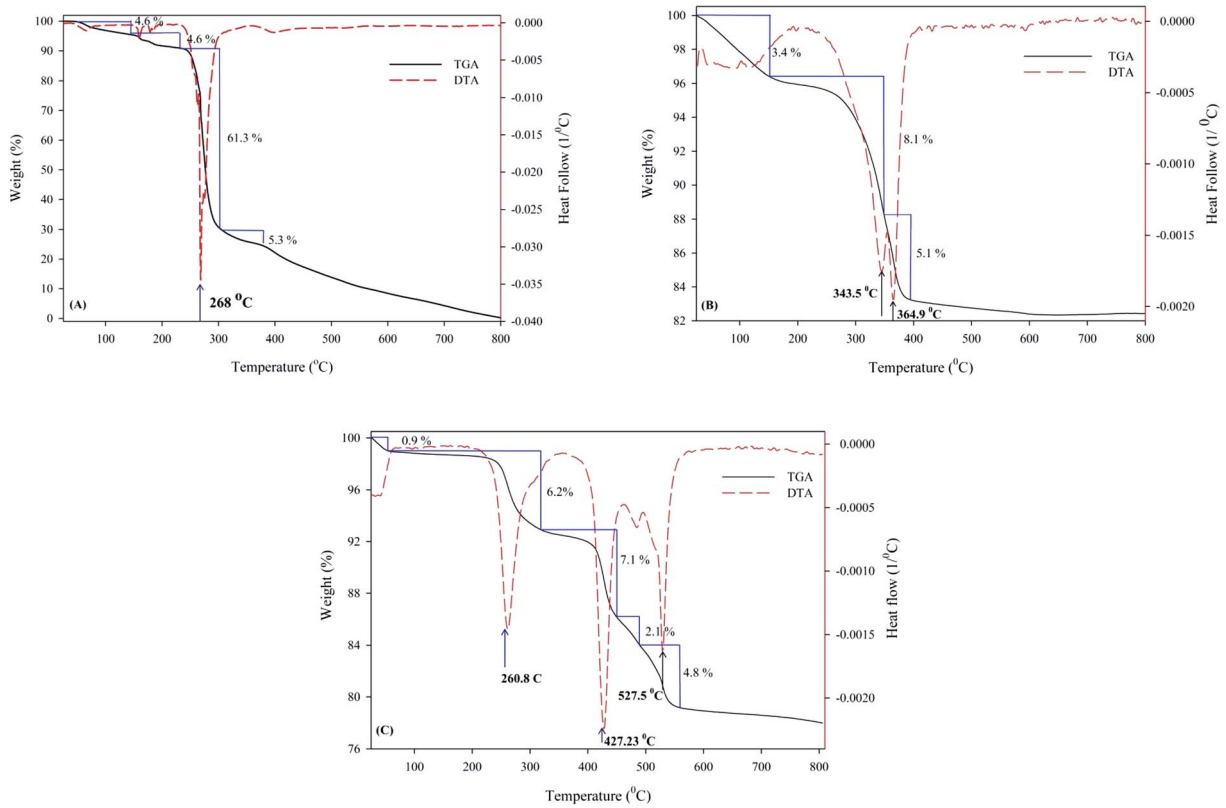

Fig. 2 TGA-DTA curves of (A) bdpy, (B) $SiW_{11}Ni$, and (C) (bdpy)$SiW_{11}Ni$/GO in the temperature range of 25–800 °C at a heating rate of 10 °C min^{-1}.

slight weight loss (0.9%) has appeared at 25–50 °C temperature range. Above 250 °C, two steps in weight loss 6.2% at 261 °C, and 14% at the temperature range of 331–557 °C are observed, correlated to the oxidative decomposition of bdpy, and GO, respectively.

The ATR-FTIR and UV-vis studies were also carried out, as shown in ESI (Fig. S1, Table S1, and Fig. S2).†

The TEM images of the GO and (bdpy)$SiW_{11}Ni$/GO at different magnifications were presented in Fig. 3. TEM images of (bdpy)$SiW_{11}Ni$/GO exhibit that (bdpy)$SiW_{11}Ni$ nanospheres were dispersed homogeneously on the GO surface. Indeed, such homogeneous dispersal of the (bdpy)$SiW_{11}Ni$ nanospheres on the surface of GO enhanced the electrochemical activity.

3.2. FE-SEM/EDS characterization of (bdpy)$SiW_{11}Ni$/P-ERGO/GCE

The surface morphology of the (bdpy)$SiW_{11}Ni$/P-ERGO/GCE was characterized by FE-SEM. The FE-SEM images of the bare GCE (Fig. 4A(a and b)) have smooth and mirror surface, which was converted to heterogeneously and crudely surface after the modification with (bdpy)$SiW_{11}Ni$/P-ERGO (Fig. 4B(a and b)). Furthermore, the EDS of the bare and modified GCE are displayed in Fig. 4A and B(c), respectively. The EDS spectra and elemental mappings approve the elemental composition, which confirms the presence of C, and O in the bare GCE (Fig. 4A(c–e)), and W, C, O, N, P, Si and, Ni elements on the (bdpy)$SiW_{11}Ni$/P-ERGO/GCE (Fig. 4B(c–j)).

3.3. Optimization of coating parameters

To gain a modified electrode with a rich electrochemical behavior, optimizing of experimental conditions is significantly necessary. Some essential factors, including type, and concentration of electrolyte additive were studied. These factors could have an impact on the electrochemical activity of the modified electrode. The following experiments were examined using CV in 0.1 mol L^{-1} H_3PO_4 supporting electrolyte at the potential of −1.5 V, and the deposition time 60 s.

3.3.1. Electrolyte additive type effect. Fig. 5A, shows the effect of electrolyte additive type (without additive, $SiW_{11}Ni$ additive, and bdpy additive), on the electrochemical behavior of the modified electrode. The modified surface, which is prepared in bdpy electrolyte additive (curve (c)), shows two-step redox peaks with less peak-to-peak separations (ΔE_p) and more faradaic peak currents (i_p) with respect to the case without additive (curve (a)). In contrast, no peak is observed in a similar potential range at the modified electrode in the presence of $SiW_{11}Ni$ additive (curve (b)). This phenomenon proves that bdpy ionic liquid, due to high ionic conductivity, can improve the electron transfer between the modifier and the electrode surface.

3.3.2. Electrolyte additive concentration effect. The optimum concentration of bdpy additive was studied at

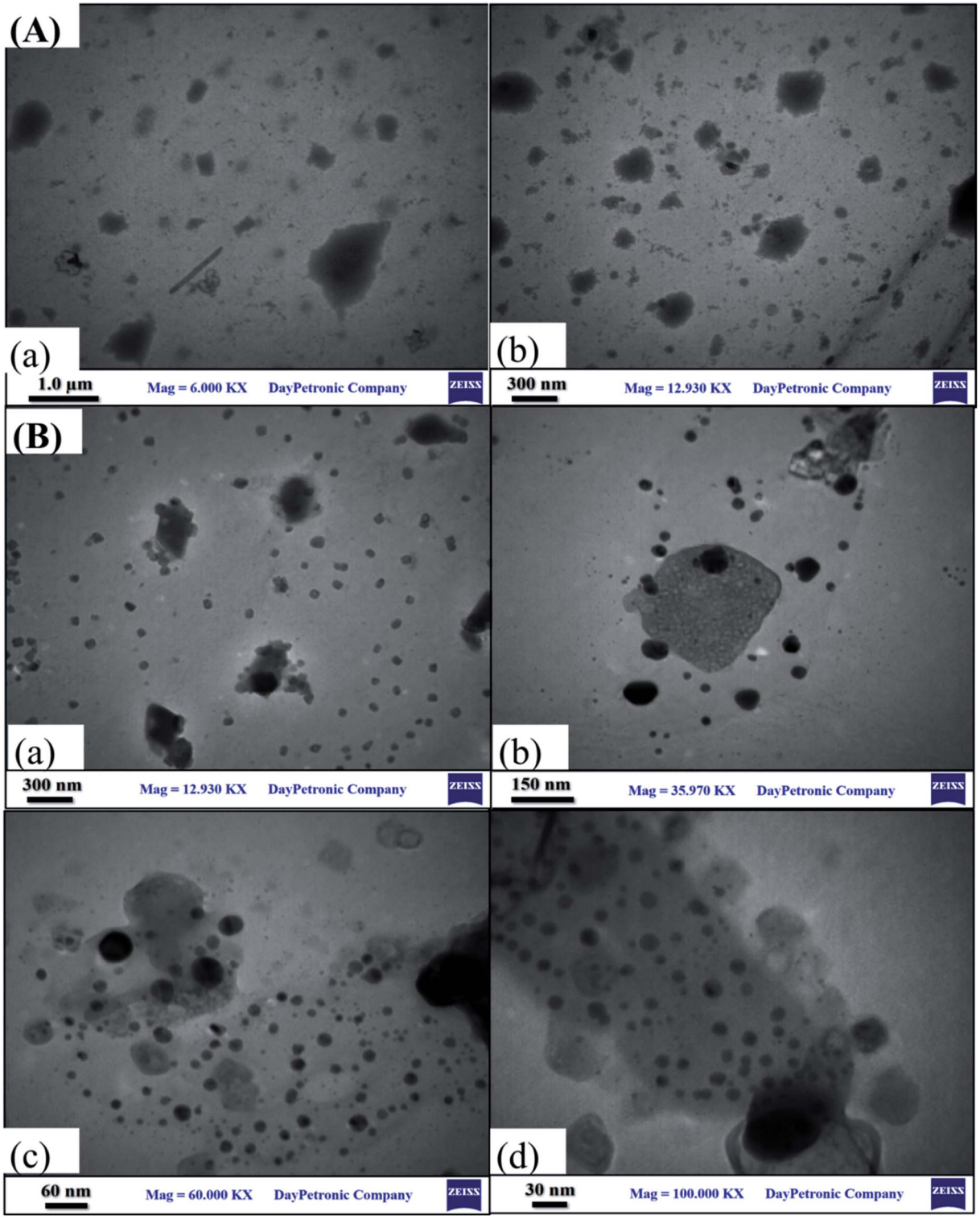

Fig. 3 TEM images of (A) GO (a and b) and (B) (bdpy)$SiW_{11}Ni$/GO (a–d) at different magnifications.

different values of 0.5, 1.0, 5.0, and 10.0 mmol L^{-1} (Fig. 5B). The maximum peak currents of the modified electrode appeared in the presence of 1.0 mmol L^{-1} bdpy additive (curve (b)). The CV signal of the modified electrode increased with bdpy concentration up to 1.0 mmol L^{-1} and then decreased (compare curve (b) with curve (c), (d)). This situation is related to the viscosity of bdpy ionic liquid. The viscosity is an essential parameter to evaluate the performance of an IL electrolyte, which directly influences the ions diffusion. Generally, high viscosity causes inferior performance. The interactions of the IL systems are through the interaction of cations and anions, leading to a significant limitation of IL electrolyte with high-viscosity.

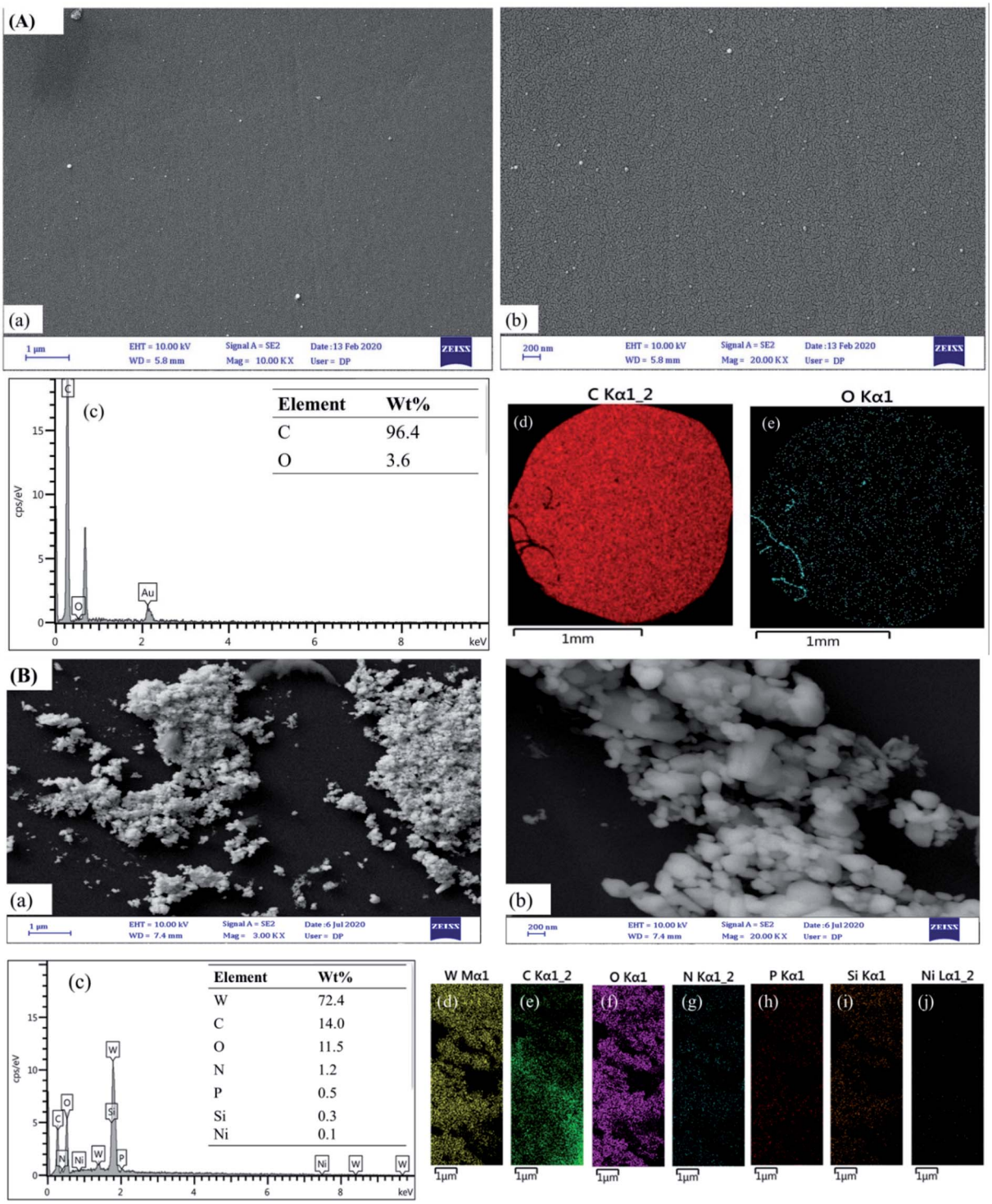

Fig. 4 (A) FE-SEM images (a and b), EDS pattern (c) and EDS element mapping (d and e) of the bare GCE and (B) FE-SEM images (a and b), EDS pattern (c) and EDS element mapping (d–j) of (bdpy)$SiW_{11}Ni$/P-ERGO/GCE.

3.4. Electrochemical behavior of (bdpy)$SiW_{11}Ni$/P-ERGO/GCE

The electrochemical properties of the bare GCE, (bdpy)$SiW_{11}Ni$/GCE, and (bdpy)$SiW_{11}Ni$/P-ERGO/GCE were studied in 0.1 mol L^{-1} $HClO_4$ electrolyte using CV technique (Fig. 6A(a–c) respectively). To better comparison, the CVs of the P-ERGO/GCE, bdpy/GCE, and $SiW_{11}Ni$/GCE were displayed in inset of Fig. 6A(d–f) respectively.

However, at the (bdpy)$SiW_{11}Ni$/GCE, and (bdpy)$SiW_{11}Ni$/P-ERGO/GCE appeared two pairs of pseudo-reversible peaks with the half-wave potentials ($E_{1/2} = (E_{pa} + E_{pc})/2$) of −529 (I–I′),

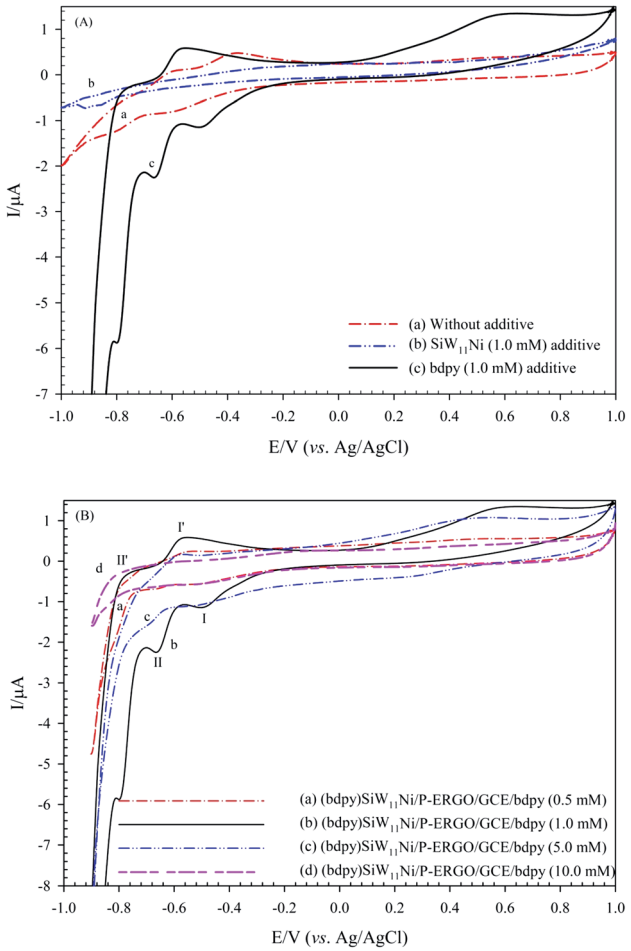

Fig. 5 Effect of (A) electrolyte additive type, (B) concentration of bdpy additive in 0.1 mol L^{-1} H_3PO_4; potential of −1.5 V; deposition time 60, on the electrochemical behavior of (bdpy)SiW_{11}Ni/P-ERGO/GCE.

and −709 (II–II′) mV respectively, that correspond to the two sequential one-electron transfer processes of $W^{6+} \rightarrow W^{5+} \rightarrow W^{4+}$. Also, as shown in Fig. 6A, there is a threefold increase of peak currents in the (bdpy)SiW_{11}Ni/P-ERGO/GCE (curve (c)) compared to the (bdpy)SiW_{11}Ni/GCE (curve (b)), and both factors confirm that the P-ERGO can promote the electron transfer between the GCE surface and the (bdpy)SiW_{11}Ni in a more effective way. In contrast, at the bare GCE (curve (a)), bdpy/GCE (curve (e)), and SiW_{11}Ni/GCE (curve (f)), no significant peak is observed under identical experimental conditions. At the P-ERGO/GCE (curve (d)), a broad redox peak appeared that was not in the potential range of electrochemical activity of (bdpy)SiW_{11}Ni.

3.4.1. Scan rate effect on the electrochemical behavior of (bdpy)SiW_{11}Ni/P-ERGO/GCE. The CVs of the (bdpy)SiW_{11}Ni/P-ERGO/GCE in $HClO_4$ (0.1 mol L^{-1}) at various scan rates (20–300 mV s^{-1}) were displayed in Fig. 6B. As shown, the cathodic peak current (peak I) increases linearly with increasing scan rate from 20 to 300 mV s^{-1} (inset of Fig. 6B) indicating the electrochemical behavior of this modified electrode is surface-controlled. Furthermore, the potential of peaks did not significantly shift with increasing scan rate, suggesting that the electron transfer kinetic was very fast on the modified electrode surface.

3.4.2. pH effect on the electrochemical behavior of (bdpy)SiW_{11}Ni/P-ERGO/GCE. The effect of buffer pH on the electrochemical behavior of the (bdpy)SiW_{11}Ni/P-ERGO/GCE was studied in 0.1 mol L^{-1} acetate buffer at different pH values (1.5–6.0), using SWV, as shown in Fig. 6C. It is clearly seen that with increased pH, the cathodic peak current (i_{pc}) reduced until no significant peak was observed at pH 6, and peak (II) potential (E_p) shifts negatively with a linear relationship of E_{pc} *vs.* pH: E_{pc} (V) = −0.052pH − 0.6896 (R^2 = 0.9976) with the slope of 52 mV/pH. The relationship between peak potential and pH, Nernst equation,[77] is described in eqn (1).

$$E_p = \frac{0.0592m}{n}\text{pH} + b \quad (1)$$

where E_p is the peak potential (V), m and n are the number of protons and electrons participating in the electrochemical reaction, respectively, and b is the intercept of the equation. From the straight line in the inset of Fig. 6C. The slope of 52 mV/pH is close to the theoretical slope value of 59 mV/pH, which means the number of protons and electrons transferred in the redox reaction of the modifier were equal.

3.5. Redox behavior of (bdpy)SiW_{11}Ni/P-ERGO/GCE in presence of $[Fe(CN)_6]^{3-/4-}$

The interfacial electron transfer properties of the bare and modified GCEs were evaluated by $[Fe(CN)_6]^{3-/4-}$ as a redox couple probe. The electron transfer kinetics of the $Fe(CN)_6^{3-/4-}$ at the interface of the modified GCEs depends on the electronic structure and thickness of the modifier.[27] As shown in Fig. 7A, curve a displays an intact pair of redox peaks at the bare GCE with a ΔE_p 102 mV and i_{pc} 2.18 μA in $Fe(CN)_6^{3-/4-}$ solution in 10 mmol L^{-1} PBS (pH 3) containing 0.1 mol L^{-1} KCl. The immobilization of SiW_{11}Ni or P-ERGO on the GCE leads to a significant increase in ΔE_p and decrease of faradaic peak currents (i_p) (Fig. 7A(b and d)). The SiW_{11}Ni or P-ERGO film serves as a barrier layer and blocks the electron transfer between $[Fe(CN)_6]^{3-/4-}$ and the surface of GCE. However, a smaller ΔE_p supplemented by an increase of i_p is found for the bdpy/GCE (Fig. 7A(c)). It indicates that the bdpy ionic liquid can improve the efficiency and rate of electron transfer at the GCE surface. The (bdpy)SiW_{11}Ni/GCE shows a greater ΔE_p than the bare GCE but smaller ΔE_p than the parent SiW_{11}Ni (Fig. 7A(e)). The better reversible behavior of (bdpy)SiW_{11}Ni *versus* SiW_{11}Ni can be credited to the presence of the bdpy ionic liquid, which owns excellent electrical conductivity.

After modification of electrode by (bdpy)SiW_{11}Ni/P-ERGO a meaning increase of ΔE_p and decrease of i_p compared with the bare GCE and also (bdpy)SiW_{11}Ni due to the presence of P-ERGO can be observed in Fig. 7A(f). The obtained quantitative information from these voltammograms is illustrated in Table 1.

The obtained CVs of (bdpy)SiW_{11}Ni/P-ERGO/GCE in 0.5 mmol L^{-1} $[Fe(CN)_6]^{3-/4-}$ at different pHs (pH 3–9) are

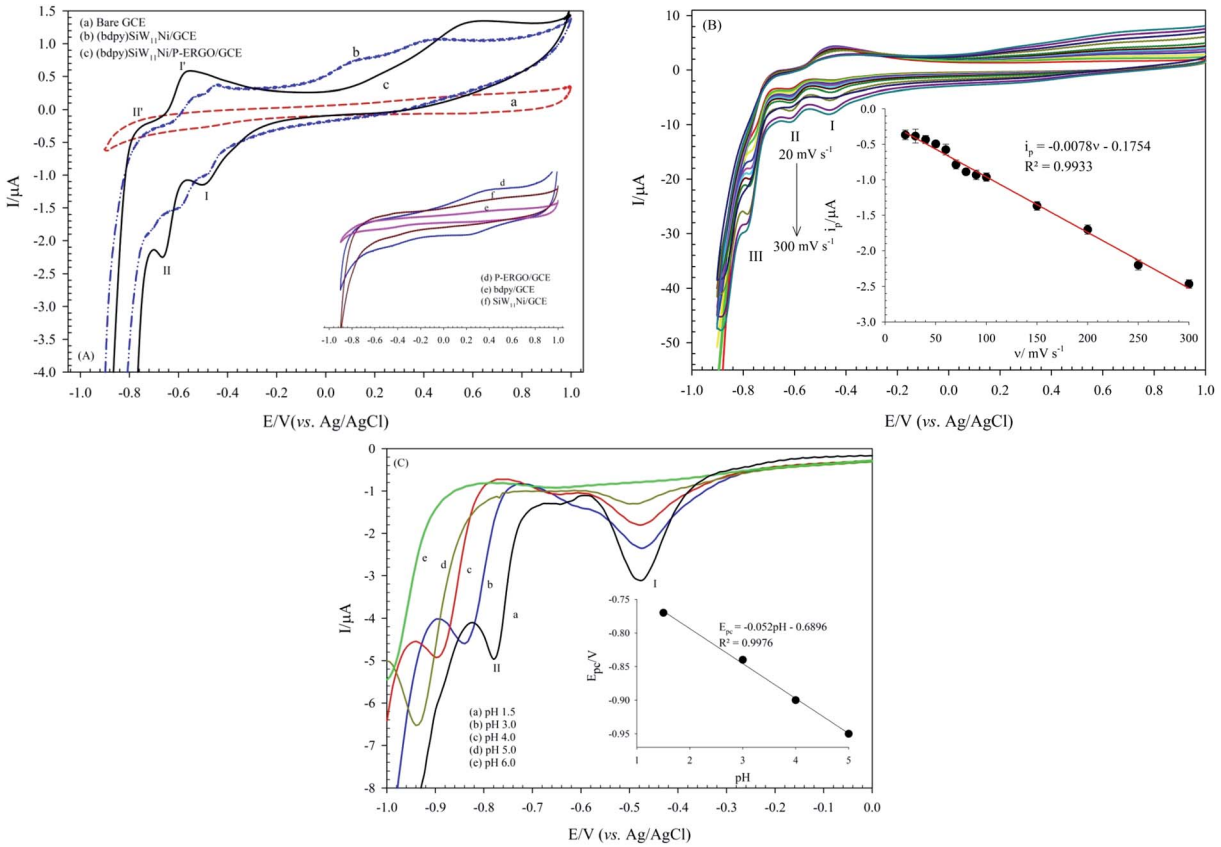

Fig. 6 (A) CVs obtained on the bare GCE (a), (bdpy)$SiW_{11}Ni$/GCE (b), (bdpy)$SiW_{11}Ni$/P-ERGO/GCE (c), P-ERGO/GCE (d), bdpy/GCE (e), and $SiW_{11}Ni$/GCE (f) in $HClO_4$ (0.1 mol L^{-1}, pH 1.5) and scan rate of 100 mV s^{-1}, (B) CV of the (bdpy)$SiW_{11}Ni$/P-ERGO/GCE in $HClO_4$ (0.1 mol L^{-1}, pH 1.5) at different scan rates from 20 to 300 mV s^{-1}. The inset shows variations of the cathodic peak I currents with scan rates, and (C) SWVs of the (bdpy)$SiW_{11}Ni$/P-ERGO/GCE in acetate buffer (0.1 mol L^{-1}) at different pHs from pH 1.5 to pH 6.0; scan rate 50 mV s^{-1}. The inset shows the variation of the cathodic peak I potentials with pHs.

Table 1 Electrochemical parameters extracted from CVs on the bare and modified GCEs in the presence of $[Fe(CN)_6]^{3-/4-}$ (0.5 mmol L^{-1}) in PBS (10.0 mmol L^{-1}, pH 3) containing KCl (0.1 mol L^{-1}) as supporting electrolyte (Fig. 7A)

Electrode	ΔE/mV ± SD[a]	i_{pc}/μA ± SD[a]	i_{pa}/μA ± SD[a]
Bare GCE	102 ± 0.10	2.18 ± 0.12	2.04 ± 0.15
$SiW_{11}Ni$/GCE	124 ± 0.11	2.01 ± 0.09	1.89 ± 0.06
bdpy/GCE	78 ± 0.09	2.20 ± 0.14	2.14 ± 0.08
P-ERGO/GCE	431 ± 2.21	0.60 ± 0.08	0.39 ± 0.04
(bdpy)$SiW_{11}Ni$/GCE	115 ± 0.83	1.18 ± 0.21	1.05 ± 0.06
(bdpy)$SiW_{11}Ni$/P-ERGO/GCE	130 ± 1.23	1.98 ± 0.09	1.75 ± 0.06

[a] SD: standard deviation (from 3 data point).

presented in Fig. 7B. As shown in Fig. 7B, with pH increasing, the i_ps decreases and the ΔE_p increases, so that at pHs above 7, almost no peak is observed. This behavior is described as follows: pH-metric titration graphs using the drawing of variation of the ΔE_p and i_p of (bdpy)$SiW_{11}Ni$/P-ERGO/GCE *versus* pH shows a surface pK_a of 5.6, and resulting, a positive charge-state of the surface at lower pH values (inset of Fig. 7B). Therefore, it can be supposed that the decreases in ΔE_p, as well as the increases in i_ps of the modified surface at acidic solutions have been affected by electrostatic interaction between the positively charged the surface of (bdpy)$SiW_{11}Ni$/P-ERGO/GCE and $[Fe(CN)_6]^{3-/4-}$ redox probe.

The effectively electroactive surface area of the (bdpy)$SiW_{11}Ni$/P-ERGO/GCE was evaluated by performing CV measurement at the (bdpy)$SiW_{11}Ni$/P-ERGO/GCE in 0.5 mmol L^{-1} $[Fe(CN)_6]^{3-/4-}$ solution in 10.0 mmol L^{-1} PBS, pH 3 PBS, pH 3 containing 0.1 mol L^{-1} KCl at different scan rates in the range of 10–150 mV s^{-1} (Fig. 7C). According to the Randles–Sevcik equation,[78,79] the surface area was calculated by eqn (2).

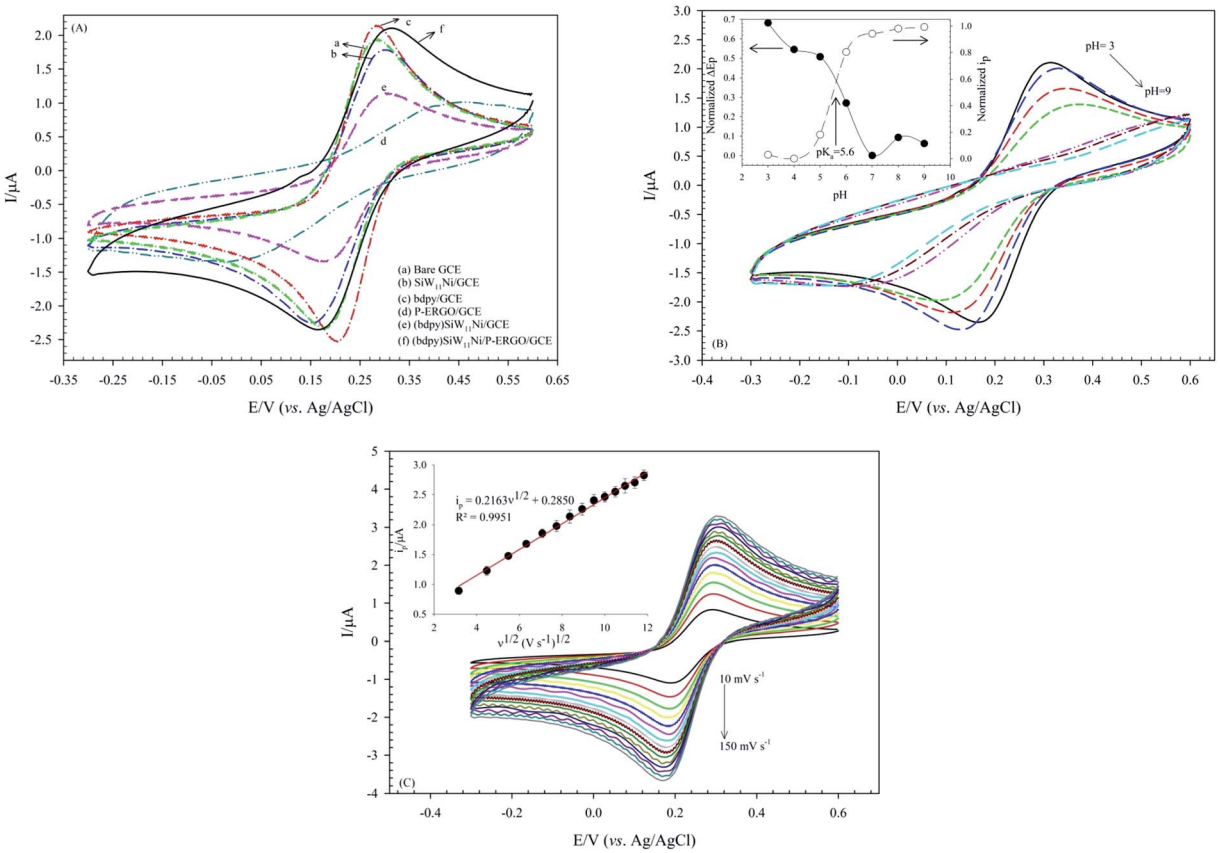

Fig. 7 CVs obtained in the presence of 0.5 mmol L^{-1} $[Fe(CN)_6]^{3-/4-}$ as a redox probe, in PBS solution (10.0 mmol L^{-1}, pH 3) containing 0.1 mol L^{-1} KCl as supporting electrolyte, (A) on the bare GCE (a), $SiW_{11}Ni$/GCE (b), bdpy/GCE (c), P-ERGO/GCE (d), (bdpy)$SiW_{11}Ni$/GCE (e), and (bdpy)$SiW_{11}Ni$/P-ERGO/GCE (f); scan rate: 50 mV s^{-1}. (B) On the (bdpy)$SiW_{11}Ni$/P-ERGO/GCE at different pHs. The inset shows the variation of normalized i_{pa} and ΔE_p extracted from CVs of (bdpy)$SiW_{11}Ni$/P-ERGO/GCE. Normalized i_{pa} and ΔE_p are $(i_{pa(max)} - i_{pa})/i_{pa(max)}$ and $(\Delta E_{p(max)} - \Delta E_p)/\Delta E_{p(max)}$, respectively. (C) On the (bdpy)$SiW_{11}Ni$/P-ERGO/GCE at different scan rates from 10 to 150 mV s^{-1}. The inset shows variations of the anodic peak currents with square root of scan rates.

$$i_p = 2.69 \times 10^5 n^{3/2} A_{eff} D_0^{1/2} \nu^{1/2} C_p \quad (2)$$

where, i_p is the peak current (A), n is the number of transferred electrons, A_{eff} is the effective surface area (cm^2), D_0 is the diffusion coefficient of $[Fe(CN)_6]^{3-/4-}$ (7.6×10^{-6} cm^2 s^{-1}), $\nu^{1/2}$ is the square root of scan rate $(V\ s^{-1})^{1/2}$, and C_p is the concentration of the probe solution (mol L^{-1}). The effective surface area of the (bdpy)$SiW_{11}Ni$/P-ERGO/GCE is calculated to be 0.588 cm^2 according to the calibration equation of $i_p = 0.2163\nu^{1/2} + 0.2850$ ($R^2 = 0.9951$) shown in inset of Fig. 7C, which is nearly 18 times larger than the bare electrode (0.0314 cm^2). However, the high electroactive surface area of the (bdpy)$SiW_{11}Ni$/P-ERGO/GCE led to enhancing the electrocatalytic activity, which is confirmed in the following part.

3.6. Electrocatalytic properties of (bdpy)$SiW_{11}Ni$/P-ERGO/GCE

The electrocatalytic activity of the (bdpy)$SiW_{11}Ni$/P-ERGO/GCE for IO_3^- electro-reduction was investigated by CV technique in 0.1 mol L^{-1} $HClO_4$ aqueous solution (pH 1.5) containing different concentrations of IO_3^- (Fig. 8A). With the increasing concentrations of IO_3^-, the cathodic peak current at about −0.45 V (peak I) of the nanocomposite modified electrode gradually increased, whereas the corresponding oxidation peak current decreased, suggesting that (bdpy)$SiW_{11}Ni$/P-ERGO/GCE would have a potential ability in the detection of IO_3^-. However, the CV method, due to essential defects such as low sensitivity and a high limit of detection (LOD), is insufficient for quantitative chemical analysis. Therefore, SWV and amperometry techniques, which benefit from low LOD and high sensitivity (small influence of background in analytical signal), were used for the sensitive measurement of IO_3^- at (bdpy)$SiW_{11}Ni$/P-ERGO/GCE.

3.6.1. Determination of IO_3^- by SWV. The SWV responses to IO_3^- of the (bdpy)$SiW_{11}Ni$/P-ERGO/GCE in 0.1 mol L^{-1} $HClO_4$ (pH 1.5) were recorded in Fig. 8B. Calibration curve for quantification of IO_3^- was obtained by plotting the dependence of peak I current *vs.* concentration of IO_3^- ($[IO_3^-]$) under optimum experimental conditions (Fig. 8C). The proportional increase of the i_p values with increasing $[IO_3^-]$ was observed in the two linear ranges of 10–400 μmol L^{-1} and 400–1000 μmol L^{-1} with linear regression equations of i_p (μA) = 0.0055$[IO_3^-]$ (μmol L^{-1}) + 0.1149 ($R^2 = 0.9947$), and i_p (μA) = 0.0014$[IO_3^-]$ (μmol L^{-1}) +

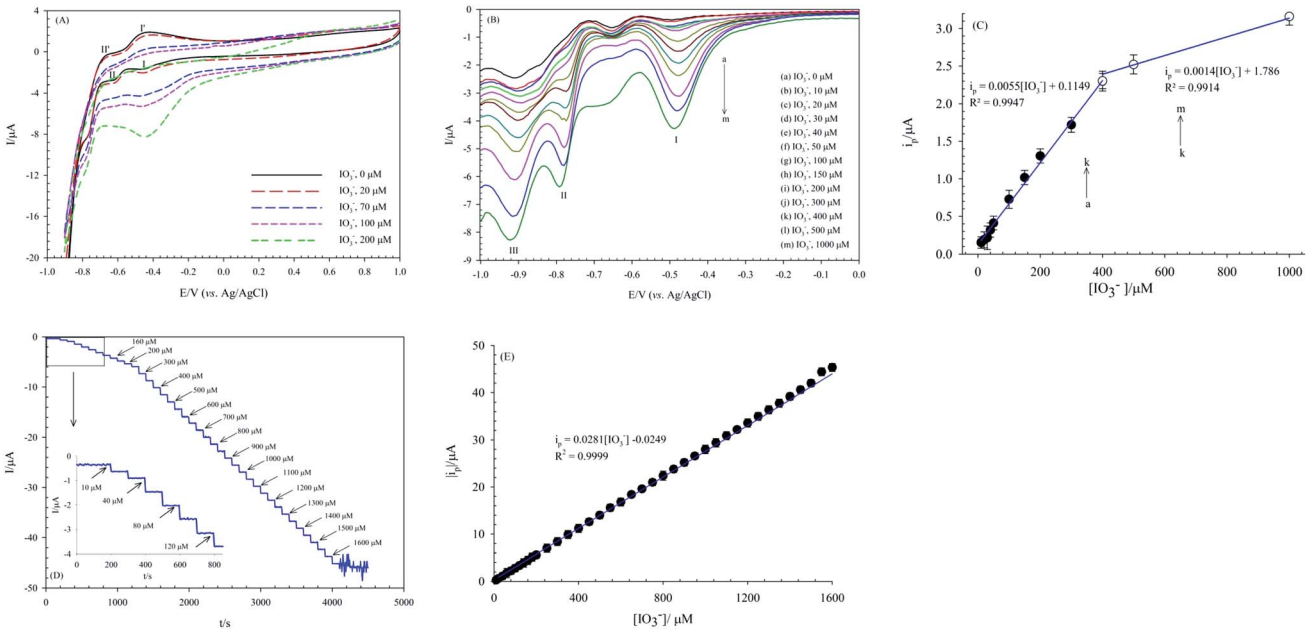

Fig. 8 (A) CVs of the (bdpy)SiW_{11}Ni/P-ERGO/GCE with different concentrations of IO_3^- in $HClO_4$ aqueous solution (0.1 mol L^{-1}, pH 1.5); scan rate 50 mV s^{-1}. (B) SWV responses for the determination of IO_3^- in the concentration ranges of 0–1000 μmol L^{-1} in $HClO_4$ aqueous solution (0.1 mol L^{-1}, pH 1.5) at (bdpy)SiW_{11}Ni/P-ERGO/GCE; scan rate 50 mV s^{-1}. (C) Corresponding calibration plot for IO_3^- (peak I). (D) Current–time responses of (bdpy)SiW_{11}Ni/P-ERGO/GCE in $HClO_4$ aqueous solution (0.1 mol L^{-1}, pH 1.5) at −0.40 V with an increasing of IO_3^- concentration. (E) Corresponding calibration plot of the absolute value of steady-state currents obtained against concentrations of IO_3^-.

Table 2 Comparative characteristics of the proposed sensor and some other electrodes for the determination of IO_3^-

Modified electrode	Sweep mode	Potential/V (*vs.* Ag/AgCl)	Linear range/ μM	LOD/μM	Sensitivity/ μA mM^{-1}	Ref.
PMo_{12}-doped sol–gel film on GCE	Amperometry	−0.24	5–6000	1	8	80
$CoW_{11}Co/PVP^a/TiO_2$/GCE	Amperometry	−0.50	2–280	0.8	N.R.[b]	81
Fe(III)P/MWCNTs/GCE	Amperometry	−0.15	10–4000	2.5	1.5	82
P_2Mo_{18}/OMC[c]/GC	Amperometry	0.00	1.13–6250	0.377	1.51	83
PMo_{12} modified CILE[d] using $[C_8Py][PF_6]$	Amperometry	0.08	10–1000	2.6	6.3	84
GCE/MWCNTs/$[C_8Py][PF_6]$-PMo_{12}	Amperometry	0.00	20–200	15	14	85
Ag/PMo_{12}/PBz[e]/GCE	Amperometry	−0.03	N.R.	1.45	0.57	86
Attapulgite/PANI[f]/PMo_{12}/GCE	Amperometry	0.00	2–520	0.53	300	87
$[PEI^g/PSS^h$-Cu@AgNPs/PEI/$P_8W_{48}]_5$/ITO[i]	Amperometry	−0.50	0.1–300	0.04	5.52	88
Fe(II)-NClin[j]-CPE[k]	SWV	0.47	4–100	0.64	67	89
Carbon nanoparticles-poly(*ortho*-aminophenol)-modified electrode	Amperometry	N.R.	500–6500	10	17.14	90
PdNF[l]/TiO_2NT[m]/Ti	Amperometry	−0.85	8.0–95.2 95.2–666.6 666.6–2065.0	3.4	8.5×10^3 5.0×10^2 1.0×10^2	91
(bdpy)SiW_{11}Ni/P-ERGO/GCE	SWV	−0.47	10–400 400–1000	2.4×10^{-3} 9.3×10^{-2}	5.50 1.40	This work
	Amperometry	−0.40	10–1600	4.7×10^{-4}	28.10	

[a] Poly(4-vinylpyridine). [b] N.R.—not recorded. [c] Ordered mesoporous carbon. [d] Carbon ionic liquid electrode. [e] Polybenzidine. [f] Polyaniline. [g] Poly(ethylenimine). [h] Poly(sodium-*p*-styrenesulfonate). [i] Indium tin oxide. [j] Clinoptilolite nanoparticles. [k] Carbon paste electrode. [l] Palladium nanoflowers. [m] Titanium oxide nanotubes.

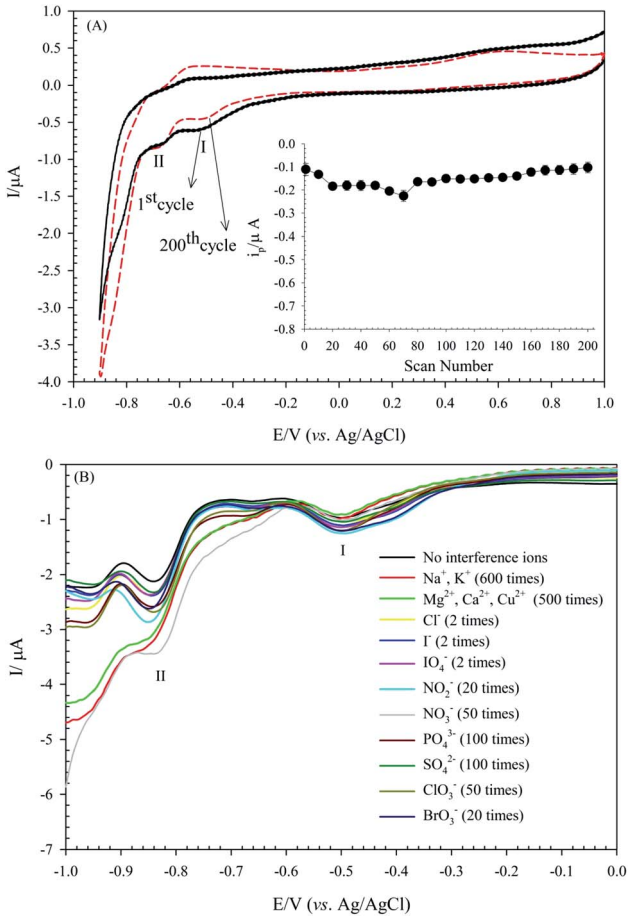

Fig. 9 (A) Stability investigation under potential cycling of (bdpy)$SiW_{11}Ni$/P-ERGO/GCE in $HClO_4$ (0.1 mol L^{-1}, pH 1.5) over 200 scans at the scan rate 50 mV s^{-1}. The inset shows variations of the cathodic peak I currents *versus* the potential scan numbers, (B) SWV responses of the (bdpy)$SiW_{11}Ni$/P-ERGO/GCE to 500 μmol L^{-1} IO_3^- in the presence of different interference ions in $HClO_4$ aqueous solution (0.1 mol L^{-1}, pH 1.5); scan rate 50 mV s^{-1}.

1.786 (R^2 = 0.9914) and limit of detections (LOD, S/N = 3) of 0.238 nmol L^{-1}, and 0.937 nmol L^{-1}, respectively.

3.6.2. Determination of IO_3^- by amperometry. Amperometry was also applied to examine the sensing characteristics of the (bdpy)$SiW_{11}Ni$/P-ERGO/GCE for determination of IO_3^- (Fig. 8D). As the IO_3^- was added into the stirred 0.1 mol L^{-1} $HClO_4$ aqueous solution (pH 1.5) at an optimum potential of −0.40 V, dynamic stairs of the current with quick steady-state were obtained, and the currents increased along with the continuous addition of IO_3^-. This can be due to the rapid diffusion of the IO_3^- small molecules from the solution to the surface of the modified electrode and the better electron transfer rate of the modifier, which can play an important role. The calibration curve presented in Fig. 8E indicated that IO_3^- sensor based on (bdpy)$SiW_{11}Ni$/P-ERGO/GCE displayed a linear response range from 10 to 1600 μmol L^{-1} with a linear regression equation of i_p (μA) = 0.0281[IO_3^-] (μmol L^{-1}) − 0.0249 (R^2 = 0.9999), LOD of 4.7 × 10^{-4} μmol L^{-1}, LOQ of 1.6 × 10^{-3} μmol L^{-1}, and sensitivity of 28.1 μA mmol L^{-1}. The LOD and LOQ were estimated by using the following equations, LOD = $3S_b/m$, and LOQ = $10S_b/m$, where S_b is the standard deviation of twenty responses of the blank solution and m is the slope of the regression line. However, at higher concentrations of 1600 μmol L^{-1}, the noise of the amperometric signal increases, and the current stabilization take longer and longer until no straight line is achieved anymore.

The linear calibration range, LOD, and sensitivity of the suggested sensor for IO_3^- determination are compared with those in previous literatures[80–91] (Table 2). The results proved that (bdpy)$SiW_{11}Ni$/P-ERGO/GCE is an excellent platform for IO_3^- detection.

The electrocatalytic behavior of the nanocomposite modified GCE towards IO_3^- can be explained by the following mechanism, that is according to previous literature:[80,81]

$$3H_4SiW_4^{V}W_7^{VI}Ni(H_2O)O_{39}^{6-} + IO_3^- \rightarrow 3H_2SiW2VW9VI\text{-}Ni(H_2O)O_{39}^{6-} + I^- + 3H_2O \quad (3)$$

$$3H_6SiW6VW5VINi(H_2O)O_{39}^{6-} + IO_3^- \rightarrow 3H_4SiW4VW7VI\text{-}Ni(H_2O)O_{39}^{6-} + I^- + 3H_2O \quad (4)$$

3.7. Stability, repeatability, and reproducibility

Achieving a high stability sensor or biosensor is one of the main goals of the analytical electrochemistry. The POMs-based modified electrodes are ordinarily stable in aqueous solutions in acidic pH. The stability of the (bdpy)$SiW_{11}Ni$/P-ERGO/GCE was evaluated by recording successive CVs at the potential range of +1.0 to −0.9 V in 0.1 mol L^{-1} $HClO_4$ solution at 50 mV s^{-1} and monitoring the changes in peak currents. As is shown in Fig. 9A, the cathodic peak I current of the modified electrode displays a small change with the current degradation of only 7.2% after 200 cycles.

Furthermore, the long-term stability experiment using SWV was also performed by keeping the (bdpy)$SiW_{11}Ni$/P-ERGO/GCE in the air at ambient conditions. The results showed that the peak I current of the modified electrode stayed at 96.12% of its primary current after ten days, 93.57% after 20 days, and

Table 3 Effect of interference ions on the detection of 500 μmol L^{-1} IO_3^-

Interference ions	$\frac{[\text{Interference ion}]}{[IO_3^-]}$	Relative signal change (%)
Na^+, K^+	600	−0.95
Cu^{2+}, Mg^{2+}, Ca^{2+}	500	−5.67
Cl^-	2.0	+5.15
I^-	2.0	+5.21
IO_4^-	2.0	+6.51
NO_2^-	20	+9.96
NO_3^-	50	+1.96
PO_4^{3-}	100	+7.58
SO_4^{2-}	100	+2.18
ClO_3^-	50	+7.82
BrO_3^-	20	+7.91

Table 4 Recovery and reliability obtained by SWV using (bdpy)$SiW_{11}Ni$/P-ERGO/GCE for the determination of IO_3^- at its various concentrations in the real samples

Sample	Originally/μM	Standard method	Spiked/μM	Found/μM	Recovery (%) ± SD[a] ($n = 3$)
1[b]	ND[c]	—	30.00	31.59	105.30 ± 1.2
		—	70.00	69.02	98.60 ± 1.6
2[d]	ND	—	20.00	21.12	105.60 ± 1.3
		—	50.00	47.39	94.78 ± 1.4
3[e]	50	56	50.00	109.80	109.80 ± 1.2
			70.00	112.74	93.95 ± 1.5

[a] Standard deviation. [b] Mineral water, from local market. [c] Not detected. [d] Tap water. [e] Commercial edible iodized salt, from local market.

91.67% after one month, indicating the excellent long-term stability of the suggested sensor.

To validate the repeatability of the (bdpy)$SiW_{11}Ni$/P-ERGO/GCE, four different voltammetry tests with one modified GCE surface were repeated in the presence of 500 μmol L^{-1} IO_3^-. Furthermore, four (bdpy)$SiW_{11}Ni$/P-ERGO/GCEs were prepared under the same conditions to compare the response currents of IO_3^-. The values of relative standard deviation (RSD) of the response currents for the repeatability and reproducibility were 3.7% and 7.8%, respectively, which demonstrated that the modified electrode has excellent repeatability and reproducibility.

3.8. Interference study

The selective response is an essential characteristic for sensors that probe the sensor-selective response to an analyte in the presence of other species. For this purpose, the potential interferences for the IO_3^- detection on this sensor were studied by adding various potential interferents into $HClO_4$ (0.1 mol L^{-1}, pH 1.5) aqueous solution through the SWV method. The results are displayed in Table 3, and Fig. 9B. These results revealed an excellent selectivity of the (bdpy)$SiW_{11}Ni$/P-ERGO/GCE nanocomposite to detect IO_3^- in complicated media.

3.9. Analytical applications for real sample

The analytical applicability of the (bdpy)$SiW_{11}Ni$/P-ERGO/GCE was validated by measuring IO_3^- content present in the mineral water (Dasani Mineral Water Co., Iran), tap water, and a commercial edible iodized salt (sample 1, 2, 3, respectively). The samples 1, and 2 were directly prepared in the $HClO_4$ solution (0.1 mol L^{-1}, pH = 1.5) without further treatment. For preparation of the sample 3, 15 mg of commercial iodized salt was dissolved in 100 mL deionized water. Then, it was diluted 27 times with 0.1 mol L^{-1} $HClO_4$ (pH = 1.5) and then poured into the electrochemical cell without any pretreatment. The content of iodate in the solution was determined by the iodometric titration method as a standard method according to the procedure given in the previous literature.[92] The measurements were performed using the standard addition method, by SWV in the potential range from 0 to −1.0 V, scan rate 50 mV s^{-1}.

The standard solutions of iodate were injected into the real samples to check the recovery percent of added iodate (found value/intrinsic value). The IO_3^- contents of iodized salt (sample 3) were compared with the values obtained by iodometric titration method as shown in Table 4, the obtained results are in good agreement with the results of the standard method with high accuracy and precision (recovery close to 100.00%). Therefore, the proposed modified electrode can be efficiently applied in detecting trace-level IO_3^- in real samples. The SWV of the (bdpy)$SiW_{11}Ni$/P-ERGO/GCE for the determination of IO_3^- in these real samples was shown in the ESI (Fig. S3).†

4. Conclusions

A new hybrid organic–inorganic nanocomposite based on POMs and RGO has been fabricated, characterized, and reported as a capable electrocatalyst in the electrochemical detection of the iodate ion. The modified electrode revealed an excellent electrocatalytic activity towards the electro-reduction of iodate ion. The high stability, good repeatability and reproducibility, as well as simplicity of electrode preparation are the features of the proposed sensor. Furthermore, the modified electrode has specific characteristics such as low LOD (4.7×10^{-4} μmol L^{-1}), high sensitivity (28.1 μA mM^{-1}), good selectivity, and wide linear range (10–1600 μmol L^{-1}) compared to other surfaces. Also, this sensor has been effectively applied for the monitoring of iodate in the real samples. All of these beneficial properties are favorable for high-performance iodate sensors.

Conflicts of interest

There are no conflicts to declare.

Acknowledgements

The authors gratefully acknowledge the financial support of this work by the Research Council of the University of Hormozgan.

References

1 Y. Tanaka, T. Hasegawa, T. Shimamura, H. Ukeda and T. Ueda, *J. Electroanal. Chem.*, 2018, **828**, 102–107.
2 L. Wang, T. Meng, J. Sun, S. Wu, M. Zhang, H. Wang and Y. Zhang, *Anal. Chim. Acta*, 2019, **1047**, 28–35.
3 M. Chi, Z. Zhu, L. Sun, T. Su, W. Liao, C. Deng, Y. Zhao, W. Ren and H. Lü, *Appl. Catal., B*, 2019, **259**, 118089.

4 Y. Jia, S. Sun, X. Cui, X. Wang and L. Yang, *Talanta*, 2019, **205**, 120139.
5 L. Jing, J. Shi, F. Zhang, Y. Zhong and W. Zhu, *Ind. Eng. Chem. Res.*, 2013, **52**, 10095–10104.
6 Q. Huang, S. Ke, L. Qiu, X. Zhang and S. Lin, *ChemCatChem*, 2014, **6**, 1531–1534.
7 S. Dianat, A. Bordbar, S. Tangestaninejad, S. Zarkesh-Esfahani, P. Habibi and A. A. Kajani, *J. Iran. Chem. Soc.*, 2016, **13**, 1895–1904.
8 S. Dianat, A.-K. Bordbar, S. Tangestaninejad, B. Yadollahi, R. Amiri, S.-H. Zarkesh-Esfahani and P. Habibi, *J. Inorg. Biochem.*, 2015, **152**, 74–81.
9 J. T. Rhule, C. L. Hill, D. A. Judd and R. F. Schinazi, *Chem. Rev.*, 1998, **98**, 327–358.
10 D.-Y. Du, J.-S. Qin, S.-L. Li, Z.-M. Su and Y.-Q. Lan, *Chem. Soc. Rev.*, 2014, **43**, 4615–4632.
11 S. Omwoma, C. T. Gore, Y. Ji, C. Hu and Y.-F. Song, *Coord. Chem. Rev.*, 2015, **286**, 17–29.
12 A. Proust, B. Matt, R. Villanneau, G. Guillemot, P. Gouzerh and G. Izzet, *Chem. Soc. Rev.*, 2012, **41**, 7605–7622.
13 Q. Wang, J. Khungwa, L. Li, Y. Liu, X. Wang and S. Wang, *J. Electroanal. Chem.*, 2018, **824**, 91–98.
14 F. Boussema, R. Haddad, Y. Ghandour, M. S. Belkhiria, M. Holzinger, A. Maaref and S. Cosnier, *Electrochim. Acta*, 2016, **222**, 402–408.
15 S. Dianat, A. Hatefi-Mehrjardi, K. Mahmoodzadeh and S. Kakhki, *New J. Chem.*, 2019, **43**, 14417–14425.
16 M. Ammam, *J. Mater. Chem. A*, 2013, **1**, 6291–6312.
17 Y. Z. Liu, W. Yao, H. M. Gan, C. Y. Sun, Z. M. Su and X. L. Wang, *Chem.–Eur. J.*, 2019, **25**, 16617–16624.
18 D. Martel, N. Sojic and A. Kuhn, *J. Chem. Educ.*, 2002, **79**, 349.
19 L. Adamczyk, *J. Solid State Electrochem.*, 2017, **21**, 211–222.
20 R. Ayranci, Y. Torlak, T. Soganci and M. Ak, *J. Electrochem. Soc.*, 2018, **165**, B638.
21 H. Yang, T. Song, L. Liu, A. Devadoss, F. Xia, H. Han, H. Park, W. Sigmund, K. Kwon and U. Paik, *J. Phys. Chem.*, 2013, **117**, 17376–17381.
22 L. Ni, G. Yang, C. Sun, G. Niu, Z. Wu, C. Chen, X. Gong, C. Zhou, G. Zhao, J. Gu, W. Ji, X. Huo, M. Chen and G. Diao, *Mater. Today Energy*, 2017, **6**, 53–64.
23 L.-H. Gao, J.-F. Zhang, H.-L. Wang, X.-Y. Lin, J.-M. Qi and K.-Z. Wang, *Electrochim. Acta*, 2015, **166**, 215–222.
24 H. Li, S. Pang, S. Wu, X. Feng, K. Müllen and C. Bubeck, *J. Am. Chem. Soc.*, 2011, **133**, 9423–9429.
25 C. P. Ponce, H. Y. Araghi, N. K. Joshi, R. P. Steer and M. F. Paige, *Langmuir*, 2015, **31**, 13590–13599.
26 J. Ni, Q.-M. Fu, L. Liu, Z.-R. Gu, Z. Zhou, F.-B. Li, S.-X. Zhang, S.-Z. Liu and Z.-L. Du, *Thin Solid Films*, 2013, **537**, 247–251.
27 S. Dianat, A. Hatefi-Mehrjardi and K. Mahmoodzadeh, *New J. Chem.*, 2019, **43**, 1388–1397.
28 M. Blasco-Ahicart, J. Soriano-López, J. J. Carbó, J. M. Poblet and J.-R. Galan-Mascaros, *Nat. Chem.*, 2018, **10**, 24–30.
29 B. Suma, P. S. Adarakatti, S. K. Kempahanumakkagari and P. Malingappa, *Mater. Chem. Phys.*, 2019, **229**, 269–278.
30 W. Guo, X. Cao, Y. Liu, X. Tong and X. Qu, *J. Electrochem. Soc.*, 2014, **161**, B248.
31 F.-Y. Yi, W. Zhu, S. Dang, J.-P. Li, D. Wu, Y.-h. Li and Z.-M. Sun, *Chem. Commun.*, 2015, **51**, 3336–3339.
32 D.-C. Zhao, Y.-Y. Hu, H. Ding, H.-Y. Guo, X.-B. Cui, X. Zhang, Q.-S. Huo and J.-Q. Xu, *Dalton Trans.*, 2015, **44**, 8971–8983.
33 J. M. Cameron, D. J. Wales and G. N. Newton, *Dalton Trans.*, 2018, **47**, 5120–5136.
34 R. Wang, D. Jia and Y. Cao, *Electrochim. Acta*, 2012, **72**, 101–107.
35 E. Rafiee and F. Mirnezami, *J. Mol. Liq.*, 2014, **199**, 156–161.
36 X. Wu, W. Wu, Q. Wu and W. Yan, *Langmuir*, 2017, **33**, 4242–4249.
37 F. Faridbod, H. Rashedi, M. R. Ganjali, P. Norouzi and S. Riahi, *Application of Room Temperature Ionic Liquids in Electrochemical Sensors and Biosensors*, INTECH Open Access Publisher, 2011.
38 N. Thakur, S. Das Adhikary, M. Kumar, D. Mehta, A. K. Padhan, D. Mandal and T. C. Nagaiah, *ACS Omega*, 2018, **3**, 2966–2973.
39 A. A. Ensafi, E. Heydari-Soureshjani, M. Jafari-Asl and B. Rezaei, *Carbon*, 2016, **99**, 398–406.
40 D. M. Fernandes, M. Nunes, B. Bachiller-Baeza, I. Rodríguez-Ramos, A. Guerrero-Ruiz, C. Delerue-Matos and C. Freire, *J. Solid State Electrochem.*, 2017, **21**, 1059–1068.
41 J. Jiao, J. Zuo, H. Pang, L. Tan, T. Chen and H. Ma, *J. Electroanal. Chem.*, 2018, **827**, 103–111.
42 G. Bajwa, M. Genovese and K. Lian, *ECS J. Solid State Sci. Technol.*, 2013, **2**, M3046.
43 L. Hong, Y. Gui, J. Lu, J. Hu, J. Yuan and L. Niu, *Int. J. Hydrogen Energy*, 2013, **38**, 11074–11079.
44 K. S. Novoselov, A. K. Geim, S. V. Morozov, D. Jiang, Y. Zhang, S. V. Dubonos, I. V. Grigorieva and A. A. Firsov, *Science*, 2004, **306**, 666–669.
45 R. Tarcan, O. Todor-Boer, I. Petrovai, C. Leordean, S. Astilean and I. Botiz, *J. Mater. Chem. C*, 2020, **8**, 1198–1224.
46 G. He, H. Chen, J. Zhu, F. Bei, X. Sun and X. Wang, *J. Mater. Chem.*, 2011, **21**, 14631–14638.
47 Y. Kim and S. Shanmugam, *ACS Appl. Mater. Interfaces*, 2013, **5**, 12197–12204.
48 N. Mizuno and M. Misono, *Chem. Rev.*, 1998, **98**, 199–218.
49 A. Ucar, M. Findik, I. H. Gubbuk, N. Kocak and H. Bingol, *Mater. Chem. Phys.*, 2017, **196**, 21–28.
50 D. M. Fernandes, M. P. Araújo, A. Haider, A. S. Mougharbel, A. J. Fernandes, U. Kortz and C. Freire, *ChemElectroChem*, 2018, **5**, 273–283.
51 J.-S. Li, Y. Wang, C.-H. Liu, S.-L. Li, Y.-G. Wang, L.-Z. Dong, Z.-H. Dai, Y.-F. Li and Y.-Q. Lan, *Nat. Commun.*, 2016, **7**, 1–8.
52 A. K. Cuentas-Gallegos, M. Lira-Cantú, N. Casañ-Pastor and P. Gómez-Romero, *Adv. Funct. Mater.*, 2005, **15**, 1125–1133.
53 J. Qin, F. Zhou, H. Xiao, R. Ren and Z.-S. Wu, *Sci. China Mater.*, 2018, **61**, 233–242.
54 H. Li, S. Pang, X. Feng, K. Müllen and C. Bubeck, *Chem. Commun.*, 2010, **46**, 6243–6245.
55 H. Li, S. Pang, S. Wu, X. Feng, K. Müllen and C. Bubeck, *J. Am. Chem. Soc.*, 2011, **133**, 9423–9429.
56 J. Chen, S. Liu, W. Feng, G. Zhang and F. Yang, *Phys. Chem. Chem. Phys.*, 2013, **15**, 5664–5669.

57 L. Cao, H. Sun, J. Li and L. Lu, *Anal. Methods*, 2011, **3**, 1587–1594.
58 D. Zhou and B.-H. Han, *Adv. Funct. Mater.*, 2010, **20**, 2717–2722.
59 W. Guo, X. Tong and S. Liu, *Electrochim. Acta*, 2015, **173**, 540–550.
60 L. Chen, Y. Tang, K. Wang, C. Liu and S. Luo, *Electrochem. Commun.*, 2011, **13**, 133–137.
61 M. Jiang, D. Zhu, J. Cai, H. Zhang and X. Zhao, *J. Phys. Chem.*, 2014, **118**, 14371–14378.
62 Y. Mai, M. Zhou, H. Ling, F. Chen, W. Lian and X. Jie, *Appl. Surf. Sci.*, 2018, **433**, 232–239.
63 M. Mirzaee, C. Dehghanian and K. S. Bokati, *J. Electroanal. Chem.*, 2018, **813**, 152–162.
64 K. Gopalakrishnan, S. Sultan, A. Govindaraj and C. Rao, *Nano Energy*, 2015, **12**, 52–58.
65 D. Zhang, Y. Zhang, Y. Luo, Y. Zhang, X. Li, X. Yu, H. Ding, P. K. Chu and L. Sun, *Nano Res.*, 2018, **11**, 1651–1663.
66 R. Ding, J. Zhang, J. Qi, Z. Li, C. Wang and M. Chen, *ACS Appl. Mater. Interfaces*, 2018, **10**, 13470–13478.
67 J. Wang, L. Shen, H. Li, X. Wang, P. Nie, B. Ding, G. Xu, H. Dou and X. Zhang, *Electrochim. Acta*, 2014, **133**, 209–216.
68 N. Lingappan and D. J. Kang, *Electrochim. Acta*, 2016, **193**, 128–136.
69 K. Bindumadhavan, P.-Y. Chang and R.-a. Doong, *Electrochim. Acta*, 2017, **243**, 282–290.
70 Z.-J. Lu, S.-J. Bao, Y.-T. Gou, C.-J. Cai, C.-C. Ji, M.-W. Xu, J. Song and R. Wang, *RSC Adv.*, 2013, **3**, 3990–3995.
71 S. Bag, B. Mondal, A. K. Das and C. R. Raj, *Electrochim. Acta*, 2015, **163**, 16–23.
72 Z. Wang, P. Li, Y. Chen, J. He, J. Liu, W. Zhang and Y. Li, *J. Power Sources*, 2014, **263**, 246–251.
73 T. Weakley and S. Malik, *J. Inorg. Nucl. Chem.*, 1967, **29**, 2935–2944.
74 D. C. Marcano, D. V. Kosynkin, J. M. Berlin, A. Sinitskii, Z. Sun, A. Slesarev, L. B. Alemany, W. Lu and J. M. Tour, *ACS Nano*, 2010, **4**, 4806–4814.
75 S. Bykkam, K. Rao, C. Chakra and T. Thunugunta, *Int. J. Adv. Biotechnol. Res.*, 2013, **4**, 142.
76 N. Raghavan, S. Thangavel and G. Venugopal, *Mater. Sci. Semicond. Process.*, 2015, **30**, 321–329.
77 L. R. Faulkner and A. J. Bard, *Electrochemical Methods: Fundamentals and Applications*, John Wiley and Sons, 2002.
78 Z. Liu, M. Jin, J. Cao, J. Wang, X. Wang, G. Zhou, A. van den Berg and L. Shui, *Sens. Actuators, B*, 2018, **257**, 1065–1075.
79 D. Zhu, H. Ma, Q. Zhen, J. Xin, L. Tan, C. Zhang, X. Wang and B. Xiao, *Appl. Surf. Sci.*, 2020, 146721.
80 W. Song, X. Chen, Y. Jiang, Y. Liu, C. Sun and X. Wang, *Anal. Chim. Acta*, 1999, **394**, 73–80.
81 Y. Li, W. Bu, L. Wu and C. Sun, *Sens. Actuators, B*, 2005, **107**, 921–928.
82 A. Salimi, H. MamKhezri, R. Hallaj and S. Zandi, *Electrochim. Acta*, 2007, **52**, 6097–6105.
83 M. Zhou, L.-p. Guo, F.-y. Lin and H.-x. Liu, *Anal. Chim. Acta*, 2007, **587**, 124–131.
84 B. Haghighi and H. Hamidi, *Electroanalysis*, 2009, **21**, 1057–1065.
85 B. Haghighi, H. Hamidi and L. Gorton, *Electrochim. Acta*, 2010, **55**, 4750–4757.
86 A. Manivel, R. Sivakumar, S. Anandan and M. Ashokkumar, *Electrocatalysis*, 2012, **3**, 22–29.
87 S. Zhang, P. He, W. Lei and G. Zhang, *J. Electroanal. Chem.*, 2014, **724**, 29–35.
88 J. Zuo, N. Gao, Z. Yu, L. Kang, K. P. O'Halloran, H. Pang, Z. Zhang and H. Ma, *J. Electroanal. Chem.*, 2015, **751**, 111–118.
89 M. Nosuhi and A. Nezamzadeh-Ejhieh, *J. Electroanal. Chem.*, 2018, **810**, 119–128.
90 J. Pishahang, H. B. Amiri and H. Heli, *Sens. Actuators, B*, 2018, **256**, 878–887.
91 F. Koohi, H. R. Zare and Z. Shekari, *Microchem. J.*, 2020, **159**, 105425.
92 M. Vithanage, I. Herath, S. Achinthya, T. Bandara, L. Weerasundara, S. Mayakaduwa, Y. Jayawardhana and P. Kumarathilaka, *Arch. Public Health*, 2016, **74**, 21.